Journal of Microelectronics and Electronic Packaging (2019) **16**, 149-156

ISSN: 1551-4897

A Capacitive Pressure Sensor Based on Cofirable Ceramic/Glass Materials with LTCC Technology

Yue Liu,[1] Yuanxun Li,[1,*] Yongcheng Lu,[1] Hua Su,[1] Zhihua Tao,[1] Mingzhou Chen,[2] and Daming Chen[3]

***Abstract*—Because of good thermal, electrical, and mechanical properties, low-temperature cofired ceramic (LTCC) has shown great potential in microelectronic applications. One of the most promising directions of LTCC technology development are integrating and packing sensors. In this article, a wireless passive capacitive pressure sensor operating in the MHz range based on cofiring of heterogeneous materials with LTCC technology is proposed, and the design, simulation, and fabrication of the sensor are demonstrated and discussed. It consists of a circular spiral inductor and a capacitor of two electrodes separated by a glass medium. Furthermore, a unique process of cofiring of heterogeneous materials was introduced to avoid deformation of the capacitive embedded cavity during lamination or sintering. The results show that the inductance of the inductor and the capacitance of the capacitor embedded in the sensor are .28 μH and 16.80 pF, respectively. The novel sensor has a sensitivity of approximately 847 Hz/MPa within the pressure range from atmospheric pressure to 100 MPa.**

***Keywords*—Capacitive pressure sensor, LTCC technology, heterogeneous materials**

Introduction

Nowadays, with the rapid development of information technology, sensors are playing an important role in information acquisition. A sensor acquires a physical signal and converts it into an electrical signal for processing. For example, pressure sensors can sense pressure and convert it into an electrical signal, whose magnitude depends on the pressure. The pressure sensor is currently being used in various fields, such as automotive, robotics, and biomedicine [1-3]. Several types of pressure sensors with different working principles have been developed [4]. Piezoresistive pressure sensors work on the principle that the change in resistance is due to the applied pressure on the sensors, and are the most common pressure sensors due to their relatively high sensitivity, broad linearity range, and low cost [5-7]. Piezoelectric pressure sensors are characterized by the piezoelectric effect, which means the sensors generate a charge when pressure is applied, and offer advantages such as easy processing, wide working frequency, and high sensitivity [8, 9]. For capacitive pressure sensors, change in electrostatic capacitance can be detected when pressure is applied, and pressure sensitivity is intrinsically high with low power consumption [10, 11]. Furthermore, the temperature effect on the characteristics of this type of sensors is negligible, and the sensors have potential application in high-temperature conditions [12]. Traditional pressure sensors, mostly made from micro-machined silicon, show great limitation when used in harsh environments, e.g., high-temperature and humid environments [13]. Low-temperature cofired ceramic (LTCC) technology is one of the microelectronic techniques that has significantly better chemical and humidity resistance than silicon-based devices. Furthermore, a large number of ceramic green tapes can be laminated and fired together to form a rigid substrate with high-density interconnections, which helps us to control the thickness of the flexible membrane to achieve a better measurement. An additional benefit of LTCC technology is the low cost compared with other technologies [14-16]. To reduce the probability of structural cracks and warpage, we chose to change the slurry formulation. By adjusting the solid content of the two materials and adjusting the shrinkage of the materials, the cofiring match of the two materials is achieved. Both the heating speed and highest temperature will influence the materials. During sintering, a high heating speed will cause device breakage and a low temperature will cause a low capacitance value. We extended the time of de-binding to slow down the volatilization of organic matter and adjusted the sintering temperature; finally, we developed a smooth device with no breakage.

An inductor is an important part of a sensor. In 2004, Pisani et al. deployed polyimide as the dielectric layer to separate a 4-μm-thick copper coil from a silicon substrate. This inductor works at a high-frequency range, but it did not have a high-Q because of the high series resistance caused by the thin coil [17]. In 2007, Wang et al. fabricated a planar racetrack copper coil surrounded by a NiFe ferromagnetic core. The embedding of this core was to support high inductance. However, despite using a 46-μm-thick coil, the maximum Q-factor was 5 at 2.5 GHz [18]. Hsueh-An developed a 10-μm-thick benzocyclobutene (BCB) along with a 10-μm-thick electroplated copper which has both a high-Q of 45 at 2.4 GHz and a high self-resonant frequency (SRF) that is above 20 GHz [19]. In 2014, Haddad's work showed that by adopting double layers, the magnetic flux of the inductor would be more constrained around the windings, and thus, a 500-nH inductor was achieved using this technique [20]. In 2015, Xiangming et al. adopted the

The manuscript was received on June 7, 2019; 1st revision received on August 13, 2019; 2nd revision received on August 18, 2019; accepted on August 19, 2019
[1]State Key Laboratory of Electronic Thin Films and Integrated Devices, University of Electronic Science and Technology of China, Chengdu 610054, China
[2]Jiangxi Guochuang Industrial Park Development Co. Ltd., Ganzhou 341400, China
[3]Institute of Electronic and Information Engineering of UESTC in Guangdong, Dongguan 523000, China
*Corresponding author; email: liyuanxun@uestc.edu.cn

doi:10.4071/imaps.926920

silicon-embedded inductors technique and combined with that an SU-8 as a low-K layer to double the performance of the inductor. This work produced a huge 5.2-μH inductance output with a Q-factor of 22 at 3.4 MHz [21].

With the development of ceramic packaging techniques, English et al. [22] proposed a wireless micro-machined ceramic pressure sensor in 1999 that can be equivalent to an inductance and capacitance (LC) resonant circuit and fabricated by LTCC technology. Because of oxidation of copper, the sensor can only work up to 200°C. Thereafter, Fonseca et al. [23] pioneered an improved model by selecting a new material (silver) instead of copper for screen printing, which made this design applicable for 400°C. In 2009, Radosavljevic et al. [24] designed a better model; the major difference between this scheme and the previously mentioned is its completely embedded circuitry, which can improve sensor reliability when operating at high temperature. In the following years, Jijun, North University of China, introduced the sacrificial layer technology to improve membrane flatness and thereby a sensor's precision [13, 25-31]. In 2018, Lin et al. [28] used a low Young's modulus LTCC material to improve sensor sensitivity without using any sacrificial material.

In this work, a wireless capacitive pressure sensor is designed based on LTCC technology with cofirable ceramic/glass materials. An inductance coil and parallel capacitor plates are embedded into a ceramic substrate to form an LC resonant circuit, which can translate pressure into a frequency shift output [32, 33]. Unlike the traditional designs, we chose a new material (glass) instead of a sacrificial layer to fill a cavity because its shrinkage more matches with that of ceramic materials and it is easy fabricated. This design is ideally suited for high-temperature, high-pressure, and low-volume sensor applications because of its intrinsic advantages.

Sensor Design

The pressure sensor principle is shown in Fig. 1. Fig. 1a shows the schematic of the contactless wireless testing concept, which is based on the transformer theory. In this study, the antenna's self-resonance frequency is higher than that of the sensor to avoid their interaction, and its transmitting frequency spectrum needs to cover the self-resonance frequency of the sensor. The impedance of the reader antenna can be expressed as [30, 33]

$$Z_{\text{eq}} = R_1 + j2\pi f L_1 \left(1 + \frac{k^2 \left(\frac{f}{f_0}\right)^2}{1 + j\frac{1}{Q_2}\frac{f}{f_0} - \left(\frac{f}{f_0}\right)^2} \right), \qquad (1)$$

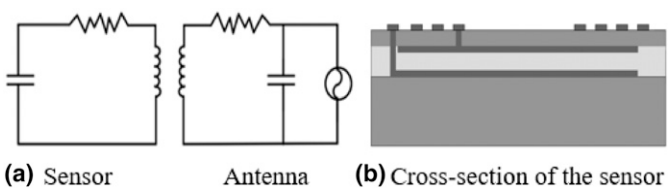

Fig. 1. (a) Schematic of the contactless wireless testing concept; (b) structural design schematic of the wireless LTCC pressure sensor.

where R_1 is the resistance of the antenna coil, L_1 is the inductance of the antenna coil, f_0 is the sensor's resonance frequency, k is the coupling coefficient, and Q_2 is the LC resonance circuit quality factor of the sensor. The reflection loss S_{11} of the readout coil is

$$S_{11} = \frac{Z_{\text{eq}} - Z_0}{Z_{\text{eq}} + Z_0}\bigg| Z_0 = 50\Omega \qquad (2)$$

When the sweep frequency is equal to the resonance frequency of the sensor, the Z_{eq} and S_{11} viewed from the testing antenna will change abruptly; by analyzing these characteristics of the antenna coil, we can detect the resonance of the sensor. Fig. 1b shows that the sensor structure consists of several different functional parts: the top part includes one layer of an LTCC tape with a circular spiral inductor on the upper surface and a square capacitor electrode on the lower surface; the middle part comprises a solid glass slip; and the bottom part is made of one layer of LTCC tape on which the lower capacitor electrode is placed. The inductor coil and the capacitor electrodes are connected by vias to form an LC circuit, and a function can be used to analyze the passive resonant circuit (LC circuit). In this circuit, inductance L_s is an invariation value, based on the parameter of the sensor shown in Table I, and the inductance is about .3 μH. The capacitor value will change if pressure P is applied to the membrane; neglecting additional fringing capacitances, C_s can be calculated using the following expression:

$$c_s = \frac{\varepsilon A}{d} = \frac{\varepsilon A}{d - \frac{1-\upsilon}{2\pi G}\oiint P^{-\frac{1}{2}} d\xi d\eta}, \qquad (3)$$

where ε is the permittivity of the glass material, and A and d are the area and space of the square electrode, respectively. It is assumed, for this scheme, that only one membrane of the sensor deflects when pressure is applied [34], where P is a uniform load, G is the elastic modulus of glass, and ν is Poisson's ratio. Finally, with a shift in resonant frequency, we can describe the change in the sensor's resonant frequency according to pressure variation using the following expression:

$$f_0 = \frac{1}{2\pi\sqrt{l_s c_s}} = \frac{1}{2\pi\sqrt{l_s \frac{\varepsilon A}{d - \frac{1-\upsilon}{2\pi G}\oiint P^{-\frac{1}{2}} d\xi d\eta}}} \qquad (4)$$

Table I
Geometrical Parameters of the Sensor

Parameters	Value
Overall dimension	15 × 15 × 0.5 mm
Capacitor electrode dimension	12 × 12 mm
Glass dimension	15mm × 15m × 0.1mm
Diameter of inner winding	8 mm
Width of winding	0.3 mm
Space between neighbor winding	0.3 mm
Number of winding	4
Thickness of the printed silver	10 um
Via dimension	0.3 × 0.3 mm

Sensor Simulation

The mathematical model does not take into account all the factors that influence the performance of the sensor; therefore, finite element modeling simulations are performed for further analysis. Here, the electromechanics interface is used to simulate the pressure-sensitive module. The geometry of the sensor is symmetric; hence, including only a single quadrant of the geometry is sufficient. A select geometric model was created using the parameters presented in Table I. We can segment the model into several functional bricks so that it is easier to change the material properties during the analysis. In this model, the terminal potential is set on the upper electrode plate and the ground plane is set on the lower electrode plate. The mechanical boundaries include fixed constraints and the size and position of the load applied. We set the lower surface of the bottom layer as a fixed surface and the upper surface of the top layer as the load layer. After that, we can choose to edit the mesh by automatic splitting, as shown in Fig. 2, and start the calculation [35].

Furthermore, the design and simulation of the wireless transmission were made using the radio frequency (RF) module shown in Fig. 3. A coupling antenna placed at a distance from the sensor is excited with an electrical current at different frequencies, generating electromagnetic fields which induce currents on the sensor. The sensor currents alter the electromagnetic fields of the antenna until the system reaches a steady state. Pressure affects the impedance of the whole system, which can be measured directly on the coupling antenna. For each capacitor with a different pressure, a unique value of resonance frequency is obtained, making identification of each tested capacitor possible. To make the simulations more efficient in computational load, metallic domains were not taken into account completely. Only their external boundaries were taken into account, using the Impedance Boundary Condition of the RF module. The lumped port is set with a terminal current of 1 A. Each domain of the model was meshed separately to have finer elements in the system [36].

Fig. 4 shows the displacement of a 3D sensor model when pressure is applied. From the figure, we can see that the maximum displacement of the sensor is approximately 2 μm when 300 MPa pressure is applied. Fig. 5 presents the pressure-capacitance relation graph. As we can see from Fig. 5, an

Fig. 2. Pressure-sensitive model.

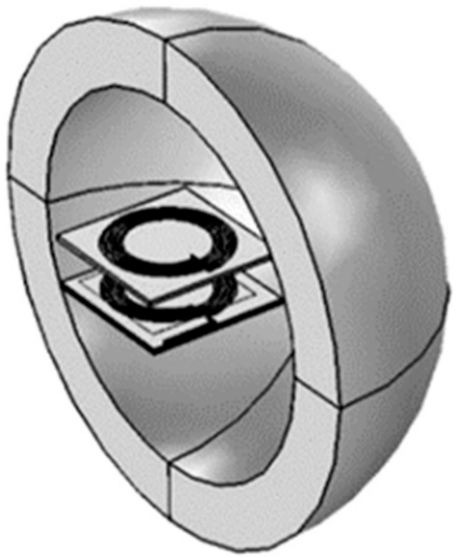

Fig. 3. Remote sensing systems.

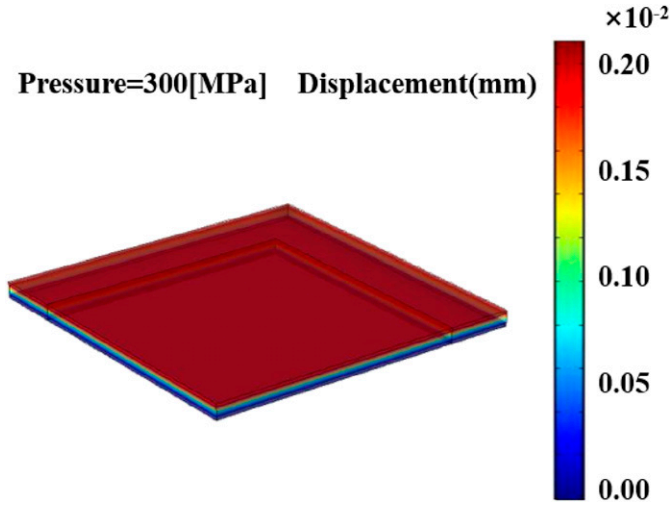

Fig. 4. Displacement of the 3D sensor model at 300 MPa pressure.

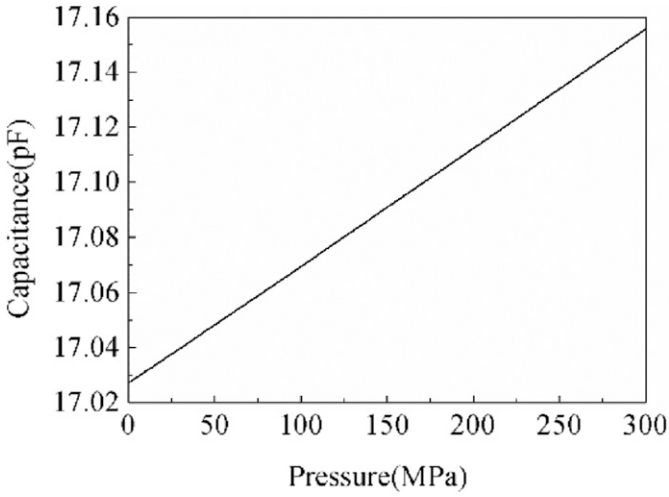

Fig. 5. Capacitance versus pressure.

increase in applied pressure results in an increase in the sensor's capacitance. The capacitance for zero pressure is 17.02 pF, and its value increases linearly when pressure increases.

Another simulation analysis has been conducted to detect the influence of sensor performance where values of geometry and material properties have been varied. To clearly describe the relationship between the behavior of sensors and the variables studied, we used the frequency shift $\Delta f = f - f_0$ to represent the frequency change; results are shown in Fig. 6. Fig. 6a shows the influence of capacitor electrode dimension on the sensor's behavior. From Fig. 6a, we can see that an increase in the dimension of the capacitor electrode reduces the sensor's sensitivity. Fig. 6b shows the influence of glass thickness on the sensor's behavior: As we can see, the sensor's sensitivity increases when the thickness of the glass increases. Fig. 6c shows that the thickness of the tape has no effect on the sensor's behavior. Fig. 6d shows the influence of the dielectric constant on the sensor's behavior: As we can see, the dielectric constant of the medium has a negative influence on the sensor's sensitivity. As shown in Fig. 6e, we can see that an increase in Poisson's ratio of the medium reduces the sensor's sensitivity. From Fig. 6f, we can see that Young's modulus has a large negative influence on the sensor's sensitivity.

Most publications focus on the optimization of the sensor element itself, and less research effort has been focused on developing an accurate readout system for wireless sensors. In this study, a wireless transmission system model is tested and optimized based on the air-core transformer under electromagnetic simulation analysis. Fig. 7 shows the real part of the equivalent input impedance $\mathrm{Re}\{Z\}$, the return loss S_{11}, and the phase of equivalent input impedance $<Z$ (at zero pressure) simulated by the RF module. Because of the sensor's coupled

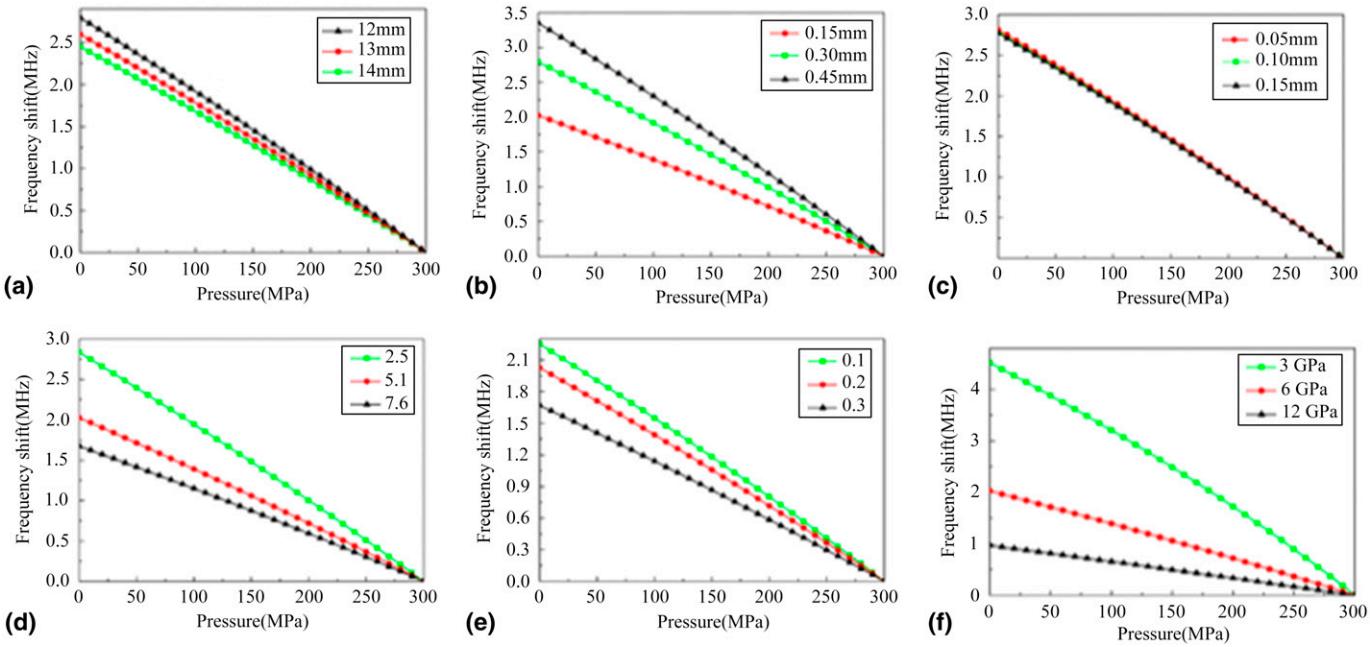

Fig. 6. (a) Pressure versus frequency for different values of capacitor electrode dimension, (b) pressure versus frequency for different values of media thickness, (c) pressure versus frequency for different values of tape thickness, (d) pressure versus frequency for different values of the dielectric constant, (e) pressure versus frequency for different values of Poisson's ratio, and (f) pressure versus frequency for different values of Young's modulus.

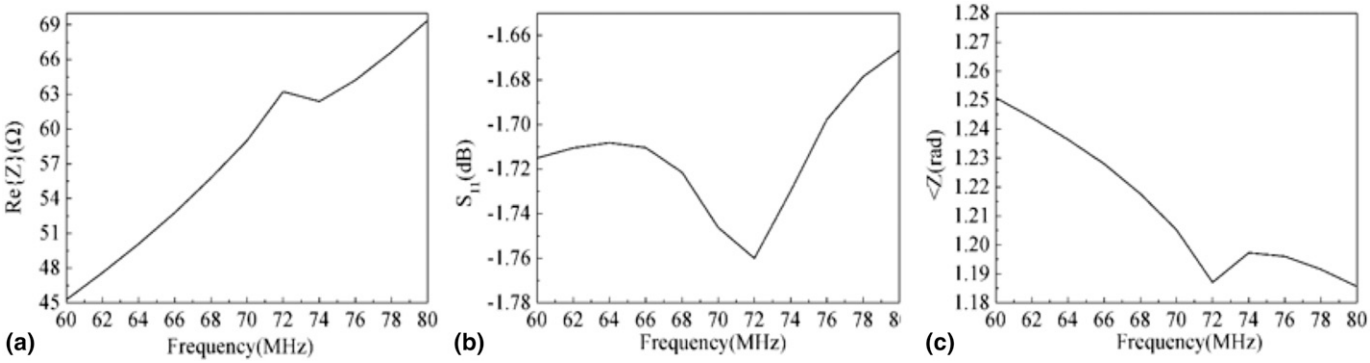

Fig. 7. (a) The real part of impedance. (b) The return loss. (c) The phase of impedance.

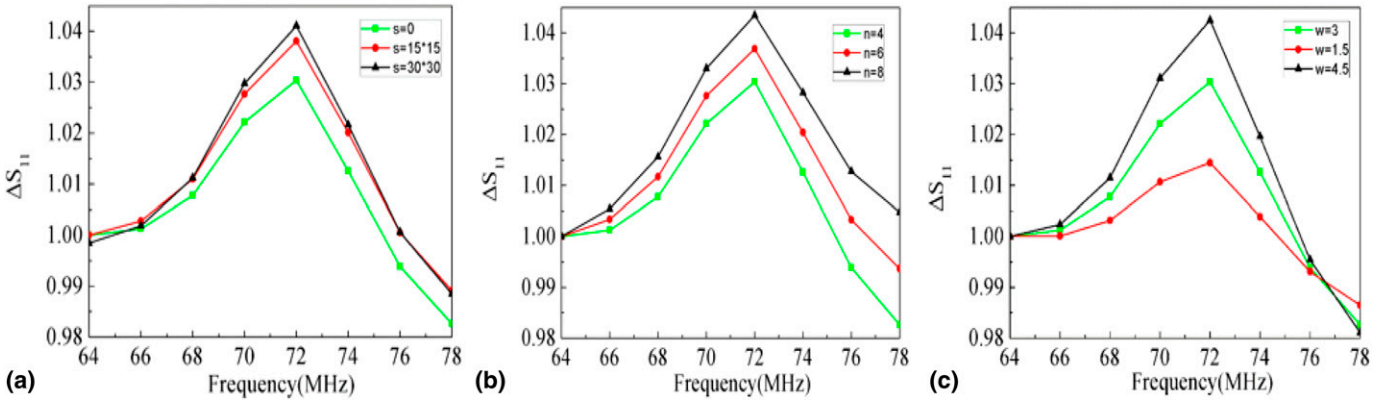

Fig. 8. (a) Return loss versus frequency under different sizes of ferrites. (b) Return loss versus frequency under different numbers of turns of the antenna coil. (c) Return loss versus frequency under different widths of the antenna coil.

Table II
Characteristics of Tape and Glass

Parameters	Tape value	Glass value
Young's modulus (GPa)	128	30
Poisson's ratio	.28	.21
Relative permittivity	18	5.1
Density (kg/m^2)	2,900	2,210

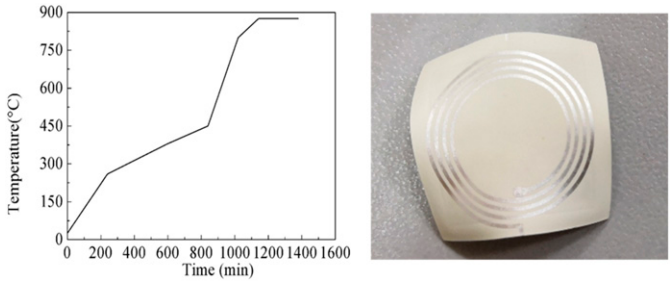

Fig. 9. (a) Temperature curve. (b) Sample 1.

effect, Re{Z}, S_{11}, and $<Z$ of the antenna abruptly changed when $f = f_0$. The simulated sensor's f_0 is 72.2 MHz at zero pressure. The impedance phase and real part showed a small change, whereas the return loss showed lot of changes; hence, we chose S_{11} parameter to measure.

This study simulates the influence of coil size and magnetic block size on the antenna return loss, where the magnet block is placed directly behind the antenna. We used the return loss shift $\Delta S_{11} = S_{11}/S_{11\_0}$ to represent S_{11} change, and S_{11_0} is the return loss parameter at 64 MHz, and the results are shown in Fig. 8. Fig. 8a shows the influence of ferrites' dimension on antenna behavior. It can be seen that the return loss curve is much better when using a magnetic block, but the influence of the continued increase in magnetic block size on the return loss curve will be reduced. Fig. 8b shows the influence of number of turns of the antenna coil on the antenna behavior. It can be seen that as the number of turns of the antenna coil increased, the return loss dip increased. As shown in Fig. 8c, an increase in the width of the antenna coil increased the return loss dip.

Fabrication

We used the traditional LTCC technology, which includes shaping of green tapes, screen printing of circuit pattern, stacking, laminating, and cofiring, to fabricate a sensor. Laboratory-made ceramics and glass were selected for the experiments, whose characteristics are shown in Table II. Ferro ME0605 Ag paste was used for sensor preparation by screen printing because its shrinkage rate is similar to that of the tape. The tapes are structured and punched through a laser machine, stenciled onto circuit pads by screen printing, laminated, and stacked the tapes into a furnace. Heterogeneous material matching cofiring technology is considered as the most important process for fabricating a pressure sensor, which eliminates collapse or pre-defection of the sensitive membrane during sintering and improves the measurable range and reliability of the sensor. To meet our requirement, we placed the stack into the furnace for cofiring with a suitable temperature curve.

In the process of sintering, it is necessary to go through the steps of heating, heat preservation, and cooling. The heating speed and highest temperature will both influence the materials. The temperature curve is shown in Fig. 9a; when the temperature is less than 450°C, the slower heating speed is conducive to de-binding, to avoid interface warpage. Sample 1 is shown in Fig. 9b. There is a tension on the interface, which makes the device bend.

Sintering characteristics of the two materials were tested using a thermomechanical analysis (TMA) tester, and the results are shown in Fig. 10. It can be seen that the sintering characteristics of glass and ceramic materials do not match. The shrinkage of the two materials is close when the temperature is less than 600°C. Thereafter, the shrinkage of the ceramic material is much smaller than that of glass. Ceramic densification is mainly carried out at a temperature range of 700-850°C. The densification process of the glass material at above 600°C is slower than that of the ceramic material. In addition, the maximum densification temperature of the glass material is around 875°C. The shrinkage mismatch between the two materials causes large stresses at the interface, causing warpage of the device.

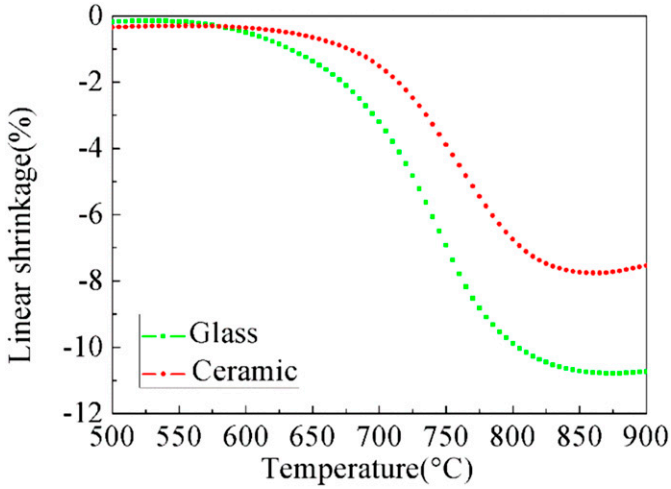

Fig. 10. TMA of glass and ceramic.

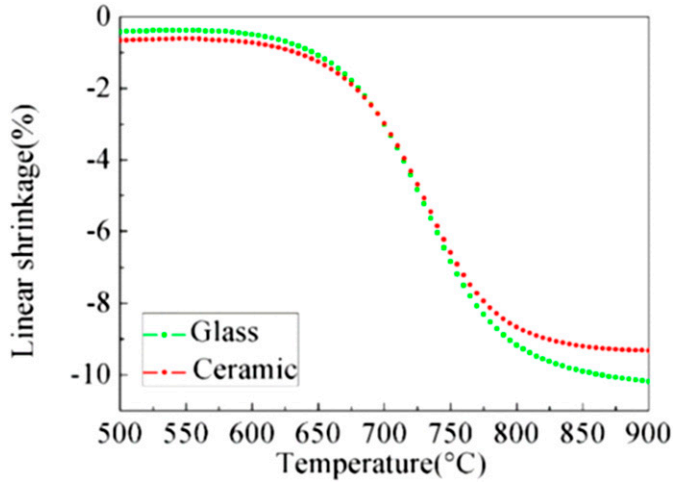

Fig. 11. TMA of glass and ceramic.

To reduce the probability of structural cracks and warpage, the shrinkage rates of the two materials need to be similar. This design starts with changing the slurry formulation. By adjusting the solid content of the two materials and adjusting the shrinkage of the materials, the cofiring match of the two materials is achieved. Organic matter is discharged during the sintering process without affecting sensor performance. We adjusted the glass and ceramic solid content during the slurry configuration process to reprocess the diaphragm. The sintering characteristics of the two materials were then retested using a TMA tester. The results are shown in Fig. 11.

The same temperature curve was used to fire sample 2, which has a new formula. Sample 2 is shown in Fig. 12. Obviously, it is smooth but a little broken.

We improve the process of sintering and obtain sample 3 as shown in Fig. 13. The green samples are initially heated to 400°C for 720 min to volatize the organic particles and then hardened by sintering to 875°C for 500 min. We extended the time of de-binding to slow down the volatilization of organic matter and adjusted the sintering temperature. Finally, we obtained a smooth device with no breakage. We further observed the structure of the sensor sample, and the result is shown in Fig. 14.

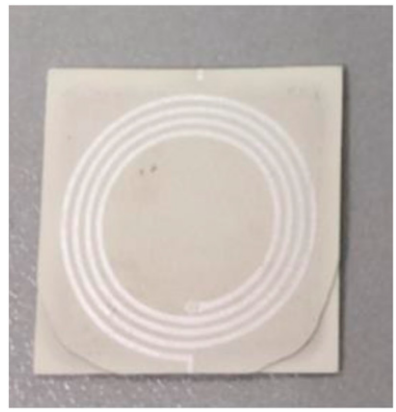

Fig. 12. Sample 2.

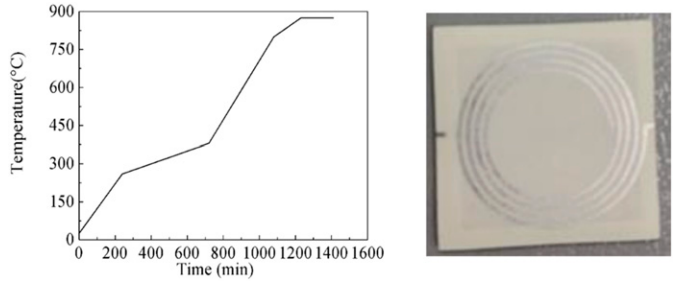

Fig. 13. (a) Temperature curve. (b) Sample 3.

Measurements and Results

Electrical parameters of three sensors were obtained by using Microtest LCR Meter 6377, and the experimental results are presented in Table III.

As can be seen from Table III, the resonance frequency of the sensor is 75.22 MHz, which is higher than the theoretical value, and the inductance and capacitance of the sensor are lower than the theoretical values. The factors are concluded as follows: (1) There is a deviation during the manufacture process. From Fig. 15a, we can see that the width of the coil is .38 mm, which is larger than the design value. (2) The dielectric constant is lower than the theoretical value. As shown in Fig. 15b, we can see that the sintering did not reach the densification and there are pores in the sample.

In our test environment, an antenna that is consistent with the spiral inductor is used to power the sensor. The antenna is connected to the network analyzer. The result on the sensor corresponds to frequency at which the network analyzer tested. Fig. 16 presents the pressure-frequency relational graph; as we can see from the graph, the sensor's sensitivity is 847 Hz/MPa, and the pressure applied ranges from 0 to 100 MPa. In Lin Lin's article, they tested four sensors and the maximum range of pressure was 0-2.5 MPa [28]. A conservative estimate is that our

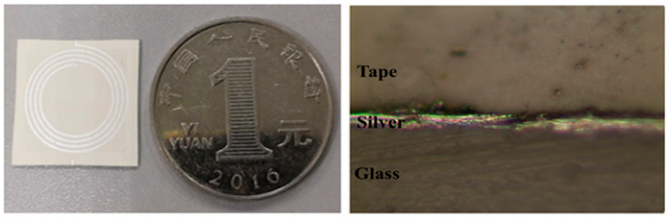

Fig. 14. (a) Completed sensor sample. (b) Cross section of the sensor.

Table III
Electrical Parameters of the Sensor

Parameters	Test value	Theoretical values
Inductance (μH)	.28	.31
Resistance (Ω)	.82	.74
Capacitance (pF)	16.81	17.03
Resonant frequency of the sensor (MHz)	75.22	72.20

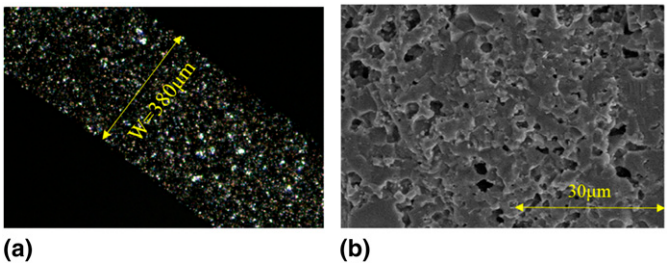

Fig. 15. (a) Spiral inductor structure. (b) scanning electron microscope (SEM) image of the glass material.

test result is more than 10 times that of Lin Lin's team. The improvement in the measurement range mainly results from the unique heterogeneous material matching cofired technology.

Conclusions

A high-performance wireless passive pressure sensor based on LTCC technology with cofirable ceramic/glass materials has been realized, where a unique heterogeneous material matching cofired technology is applied, which improves the reliability of the sensor. Parallel capacitor plates, an inductance coil, and a glass medium are embedded into the ceramic substrate to form the LC circuit. Pressure variations are monitored and detected by the change in the sensor's resonant frequency by applying wireless signal transmission. In this scheme, the sensor was tested and the results show that the inductance of the inductor and the capacitance of the capacitor embedded in the sensor are .28 μH and 16.80 pF, respectively, lower than the design value. The factor is that there is a deviation during the manufacture process. The frequency shift of the sensor versus pressure has good linearity and is approximately 847 Hz/MPa within the pressure range from atmospheric pressure to 100 MPa. In this study, the sensor has advantages of suitability for

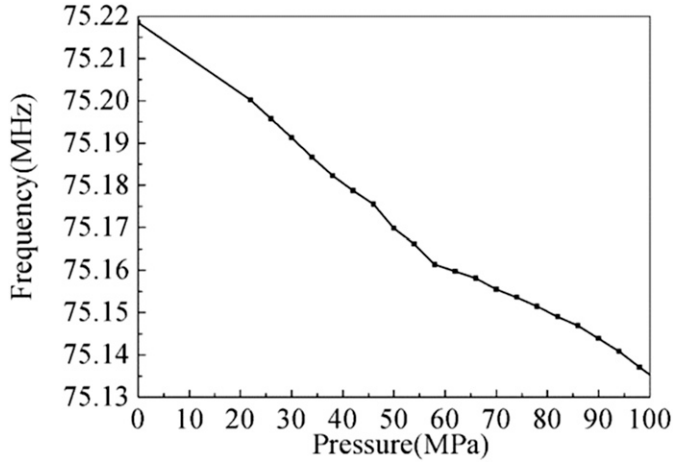

Fig. 16. Resonance frequency versus applied pressure.

high-temperature applications, a robust structure, low energy consumption, high reliability, and a large measurement range. However, the output signal has a low shift; in the future, we will optimize of the sensor geometry and material to improve the sensitivity of the sensor.

Acknowledgments

This work was supported by the Sichuan Science and Technology Project (Grant No. 2019YFG0101), Natural Science Foundation of Guangdong Province (Grant No. 2016A03031006), Guizhou science and technology major projects (Grant No. 20163011), and Dongguan entrepreneurial talent program.

References

[1] B. Adam, T. Brandt, R. Henn, S. Reiss, M. Lang, and C. Ohl, "A new micromechanical pressure sensor for automotive airbag applications," in *Advanced Microsystems for Automotive Applications 2008*, Springer, Berlin, Heidelberg, pp. 259-284, 2008.

[2] J. Müntjes, J. Häfner, M. Görtz, and W. Mokwa, "Studies on thinned flexible integrated capacitive pressure sensors in tactile sensor arrays for the use in robotics and prosthetics," Solid-State Sensors, Actuators and Microsystems, Transducers & Eurosensors XXVII: The 17th International Conference, pp. 1460-1463, Barcelona, 16 June 2013.

[3] C.-C. Chiang, C.-C.K. Lin, and M.-S. Ju, "An implantable capacitive pressure sensor for biomedical applications," *Sensors and Actuators A: Physical*, Vol. 134, pp. 382-388, 2007.

[4] D. Jurków, T. Maeder, A. Dąbrowski, M.S. Zarnik, D. Belavič, H. Bartsch, and J. Müllerd, "Overview on low temperature co-fired ceramic sensors," *Sensors and Actuators A: Physical*, Vol. 233, pp. 125-146, 2015.

[5] M. Santo Zarnik, V. Sedlakova, D. Belavic, J. Sikula, J. Majzner, and P. Sedlak, "Estimation of the long-term stability of piezoresistive LTCC pressure sensors by means of low-frequency noise measurements," *Sensors and Actuators A: Physical*, Vol. 199, pp. 334-343, 2013.

[6] M. Santo Zarnik, D. Belavic, and S. Macek, "The warm-up and offset stability of a low-pressure piezoresistive ceramic pressure Sensor," *Sensors and Actuators A: Physical*, Vol. 158, pp. 198-206, 2010.

[7] D. Belavič, M. Hodnik, M. Santo, P.F. Bolado, H. Uršič, A. Bradeško, B. Malic, I.-F. Mercioniu, A. Bencan, K. Makarovic, R. C. Ciobanu, and C. Schreiner, "LTCC-based ceramic microsystems with integrated fluidic elements and sensors," Electrical and Power Engineering (EPE), 2016 International Conference and Exposition, pp. 042-046, Denver, CO, 22-25 May 2016.

[8] M. Zarnik, D. Belavic, S. Macek, and M. Kosec, "An application of PZT thick films on LTCC substrates: a case study of a resonant pressure sensor,"

Applications of Ferroelectrics, 2008. ISAF 2008. 17th IEEE International Symposium, pp. 1-2, Santa Fe, New Mexico, 23 February 2008.

[9] M.S. Zarnik, D. Belavič, S. Maček, and J. Holc, "Feasibility study of a thick-film PZT resonant pressure sensor made on a prefired 3D LTCC structure," *International Journal of Applied Ceramic Technology*, Vol. 6, pp. 9-17, 2009.

[10] C. Li, Q. Tan, W. Zhang, C. Xue, Y. Li, and J. Xiong, "Microfabrication of a novel ceramic pressure sensor with high sensitivity based on low-temperature co-fired ceramic (LTCC) technology," *Micromachines*, Vol. 5, pp. 396-407, 2014.

[11] D. Belavic, M. Santo Zarnik, S. Macek, M. Jerlah, M. Hrovat, and M. Pavlin, "Capacitive pressure sensors realized with LTCC technology," Electronics Technology, 2008. ISSE'08. 31st International Spring Seminar, pp. 269-272, Budapest, Hungary, 7 May 2008.

[12] O. Akar, T. Akin, and K. Najafi, "A wireless batch sealed absolute capacitive pressure sensor," *Sensors and Actuators A: Physical*, Vol. 95, pp. 29-38, 2001.

[13] T. Qiulin, K. Hao, Q. Li, X. Jijun, L. Jun, X. Chenyang, Z. Wendong, and L. Tao, "High temperature characteristic for wireless pressure LTCC-based sensor," *Microsystem Technologies*, Vol. 21, pp. 209-214, 2015.

[14] L. Golonka, "Technology and applications of low temperature cofired ceramic (LTCC) based sensors and microsystems," *Bulletin of the Polish Academy of Sciences, Technical Sciences*, Vol. 54, pp. 247-260, 2006.

[15] U. Partsch, C. Lenz, S. Ziesche, C. Lohrberg, H. Neubert, and T. Maeder, "LTCC-based sensors for mechanical quantities," *Journal of Mcroelectronics, Electronic Components and Materials*, Vol. 42, pp. 260-271, 2012.

[16] M.R. Gongora-Rubio, P. Espinoza-Vallejos, L. Sola-Laguna, and J. Santiago-Aviles, "Overview of low temperature co-fired ceramics tape technology for meso-system technology (MsST)," *Sensors and Actuators A: Physical*, Vol. 89, pp. 222-241, 2001.

[17] M.B. Pisani, C. Hibert, D. Bouvet, P. Beaud, and A.M. Ionescu, "Copper/polyimide fabrication process for above-IC integration of high quality factor inductors," *Microelectronic Engineering*, Vol. 73-74, pp. 474-479, 2004.

[18] H.-A. Yang, C.-C. Wang, P.-J. Zheng, and W.-C. Wang, "On-chip high-Q inductor using wafer-level chip-scale package technology," Proceedings of the IEEE International Microsystems, Packaging, Assembly and Circuits Technology, Assembly Circuits Technology Conference (IMPACT), pp. 173-176, Taipei, Taiwan, 1-3 October 2007.

[19] X. Fang, T.H. Mak, Y. Gao, K.M. Lau, P.K.T. Mok, and J. K. O. Sin, "A low substrate loss, monolithically integrated power inductor for compact LED drivers," Proceedings of the IEEE 27th International Symposium Power Semiconductor Devices IC's (ISPSD), pp. 53-56, Hong Kong, China, 10 May 2015.

[20] N. Wang, T. O'Donnell, S. Roy, P. McCloskey, and C. O'Mathuna, "Micro-inductors integrated on silicon for power supply on chip," *Journal of Magnetism and Magnetic Materials*, Vol. 316, No. 2, pp. e233-e237, 2007.

[21] E. Haddad, Christian Martin, Charles Joubert, Bruno Allard, Cyril Buttay, Tony Abi Tannous, and Pascal Bevilacqua, "Planar, double-layer magnetic inductors for low power, high frequency DC-DC converters," Proceedings of the 8th International Conference on Integrated Power Electronics Systems (CIPS), February 2014, pp. 1-5, Nuremberg, Germany, 25 February 2014.

[22] J.M. English and M.G. Allen, "Wireless micromachined ceramic pressure sensors," Micro Electro Mechanical Systems, 1999. MEMS'99. Twelfth IEEE International Conference, pp. 511-516, Orlando, FL, 21 January 1999.

[23] M.A. Fonseca, J.M. English, M. Von Arx, and M.G. Allen, "Wireless micromachined ceramic pressure sensor for high-temperature applications," *Journal of Microelectromechanical Systems*, Vol. 11, pp. 337-343, 2002.

[24] G.J. Radosavljevic, L.D. Zivanov, W. Smetana, A.M. Maric, M. Unger, and L.F. Nad, "A wireless embedded resonant pressure sensor fabricated in the standard LTCC technology," *IEEE Sensors Journal*, Vol. 9, pp. 1956-1962, 2009.

[25] D. Jurków, T. Maeder, A. Dąbrowski, M. Santo Zarnik, D. Belavič, H. Bartsch, and J. Müller, "Overview on low temperature co-fired ceramic sensors," *Sensors and Actuators A: Physical*, Vol. 233, pp. 125-146, 2015.

[26] J. Xiong, Y. Li, Y. Hong, B. Zhang, T. Cui, Q. Tan, S. Zheng, and T. Liang, "Wireless LTCC-based capacitive pressure sensor for harsh environment," *Sensors and Actuators. A, Physical*, Vol. 197, pp. 30-37, 2013.

[27] L. Qin, D. Shen, T. Wei, Q. Tan, T. Luo, Z. Zhou, and J. Xiong, "A wireless passive LC resonant sensor based on LTCC under high-temperature/pressure environments," *Sensors (Basel)*, Vol. 15, pp. 16729-16739, 2015.

[28] L. Lin, M. Ma, F. Zhang, F. Liu, Z. Liu, and Y. Li, "Fabrications and performance of wireless LC pressure sensors through LTCC technology," *Sensors (Basel)*, Vol. 18, p. 340, 2018.

[29] C. Li, Q. Tan, C. Xue, W. Zhang, Y. Li, and J. Xiong, "A high-performance LC wireless passive pressure sensor fabricated using low-temperature co-fired ceramic (LTCC) technology," *Sensors (Basel)*, Vol. 14, pp. 23337-23347, 2014.

[30] Q. Tan, C. Li, J. Xiong, P. Jia, W. Zhang, J. Liu, C. Xue, Y. Hong, Z. Ren, and T. Luo, "A high temperature capacitive pressure sensor based on alumina ceramic for in situ measurement at 600°C," *Sensors (Basel)*, Vol. 14, pp. 2417-2430, 2014.

[31] Q. Tan, T. Luo, T. Wei, J. Liu, L. Lin, and J. Xiong, "A wireless passive pressure and temperature sensor via a dual LC resonant circuit in harsh environments," *Journal of Microelectromechanical Systems*, Vol. 26, pp. 351-356, 2017.

[32] S.C. Mannsfeld, B.C. Tee, R.M. Stoltenberg, C.V.H. Chen, S. Barman, B.V. Muir, A.N. Sokolov, C. Reese, and Z. Bao, "Highly sensitive flexible pressure sensors with microstructured rubber dielectric layers," *Nature Materials*, Vol. 9, p. 859, 2010.

[33] M.A. Fonseca, "Polymer/ceramic wireless MEMS pressure sensors for harsh environments: high temperature and biomedical applications," Georgia Institute of Technology, Georgia Institute of Technology North Avenue, Atlanta, GA, 2007.

[34] K.F. Lei, K.-F. Lee, and M.-Y. Lee, "Development of a flexible PDMS capacitive pressure sensor for plantar pressure measurement," *Microelectronic Engineering*, Vol. 99, pp. 1-5, 2012.

[35] C. Marghescu, C. Ionescu, P. Svasta, M. Santo Zarnik, and D. Belavič, "FE modeling of capacitive pressure sensors realized in LTCC technology," Electronics Technology (ISSE), 2010 33rd International Spring Seminar, pp. 350-353, Warsaw, Poland, 12 May 2010.

[36] D.A. Sanz, C. Mitrosbaras, E.A. Unigarro, and F. Segura-Quijano, "Passive resonators for wireless passive sensor readout enhancement," *Applied Physics Letters*, Vol. 103, p. 133502, 2013.